Sea ice production in the 2016 and 2017 Maud Rise polynyas

Lu Zhou [1], **Céline Heuzé** [1], **Martin Mohrmann** [2]

[1]Department of Earth Sciences, University of Gothenburg, Gothenburg, Sweden
[2]Department of Marine Sciences, University of Gothenburg, Gothenburg, Sweden

Key Points:

- Large ice production is found in the 2016 and 2017 Maud Rise open-ocean polynyas, as large as the second largest productive coastal polynyas
- Heat flux from the upper ocean within the polynya is calculated from in-situ measurements for the first time and larger than expected
- Sea ice production within the Maud Rise polynyas is strongly correlated to the 2 m temperature yet most sensitive to the 1000 hPa temperature

Corresponding author: Lu Zhou, lu.zhou@gu.se

Abstract

Sea ice production within polynyas, an outcome of the atmosphere - ice - ocean interaction, is a major source of dense water and hence key to the global overturning circulation, but is poorly quantified over open-ocean polynyas. Using the two recent extensive open-ocean polynyas within the wider Maud Rise region of the Weddell Sea in 2016 and 2017, we here explore the surface ice energy budget and estimate their ice production based on satellite retrievals, in-situ hydrographic observations, and the Japanese 55-year Reanalysis (JRA55). We find that the oceanic heat flux amounts to 36.1 and 30.7 W m^{-2} within the 2016 and 2017 polynyas, respectively. We find that the 2017 open-ocean polynya produced nearly 200 km^3 of new sea ice, which is comparable to the production in the largest Antarctic coastal polynyas. Finally, we find that ice production is highly correlated with the 2 m air temperature and wind speed, which affect the turbulent fluxes. It is also highly sensitive to uncertainties in the atmospheric air temperature and mixed layer depth, which urgently need to be better monitored at high latitudes.

Plain Language Summary

Polynyas, openings in the sea ice, are crucial places for sea ice formation and are often referred to as "ice factories". However, this ice production, which is critical to the formation of very dense and cold Antarctic Bottom Water (AABW), is rarely quantified for open-ocean polynyas. Here, we determine the sea ice volume produced within the latest 2016 and 2017 Maud Rise polynyas based on various satellite-retrieved observations by computing the surface heat budget. For the first time, we estimate the upper oceanic heat flux before and during a polynya from in-situ measurements within the polynya. This oceanic heat flux is crucial, as it strongly impacts ice formation. We estimate that the 2017 polynya produced an amount of ice comparable to that in the largest coastal polynyas. Finally, we find a link between air temperature, wind speed, ocean current and our estimated sea ice formation and show that the accuracy of the estimation largely depends on the near-surface atmospheric conditions. The sea ice production estimated in this study has substantial implications for AABW formation and can be used to better assess the air - ice - ocean interactions in the rapidly changing polar regions.

1 Introduction

Polynyas are regions of low sea ice concentration or thickness where the comparatively warm ocean is exposed to the cold atmosphere. Coastal polynyas are mainly driven by katabatic winds, while sensible heat convection results in open-ocean/offshore polynyas(Morales Maqueda et al., 2004). Morales Maqueda et al. (2004) (and references therein) summarized that air - ice - ocean interactions in polynyas could impact: (1) the moisture and heat exchange between atmosphere and ocean and, therefore, the local wind dynamics; (2) the upper ocean properties and vertical flows of dense saline water through brine rejection and buoyancy loss; (3) the biogeochemical fluxes, e.g. acting as the sinks of atmospheric CO_2, between air and sea; (4) the local ecosystems with extra phytoplankton and zooplankton, served as "oases" in a polar ocean desert. In the Southern Ocean, open-ocean polynyas occur rarely but can reach a large extent. Such an open-ocean polynya, the Maud Rise polynya, opened in the vicinity of the Maud Rise seamount (centered on 64°S, 3°E) in 2016 and 2017, reaching up to 100 000 km^2 (Swart et al., 2018; Jena et al., 2019; Campbell et al., 2019). As Weddell Sea polynya, it had previously reached a size of 300 000 km^2 in 1974-1976 (Carsey, 1980). In contrast, Antarctic coastal polynyas occur frequently, with a variable extent, from 130 km^2 to 20 000 km^2 (Barber & Massom, 2007). Apart from the extent, the satellites have allowed to analyze the thinning sea ice thickness anomalies within the recent two Maud Rise polynyas (Mchedlishvili et al., 2022) from the satellites.

The chain of events leading to open-ocean polynyas over Maud Rise is not yet fully understood, but various hypotheses have been suggested, including the spinup of the Weddell Gyre; the warm Circumpolar Deep Water (CDW) shoaling; salinity injection through vertical entrainment; Maud Rise topography interaction with the flow (Cheon & Gordon, 2019; Wilson et al., 2019; Zhou et al., 2022), and anomalous atmospheric dynamic stresses; positive energy surface

flux (A. L. Gordon et al., 2007; Campbell et al., 2019; Francis et al., 2019, 2020). After its opening, the polynya will remain open, changing size and position, until the heat at depth is depleted, heat loss to the atmosphere ceases, or freshwater restratifies the surface in the region (T. Martin et al., 2013; Dufour et al., 2017). However, the impact of brine rejection from sea ice production in open-ocean polynyas remains unclear and needs better quantification (A. Gordon, 1982; Francis et al., 2020). Most studies of sea ice production in the Southern Ocean have so far focused on coastal polynyas instead, which contribute as much as 10% of the total Antarctic sea ice production (Tamura et al., 2008). Moreover, ice production-related brine rejection there leads to the formation of Antarctic Bottom Water (AABW) (S. Martin et al., 2007), the densest water mass that occupies the abyssal layer of the global ocean.

As the results of air - ice - ocean interactions, several studies have recently addressed the sea ice thickness and production within the polynya through satellites. Multiple algorithms exist to retrieve thin sea ice thickness by combining L-band microwave radiometry Soil Moisture Ocean Salinity (SMOS) and Soil Moisture Active Passive (SMAP); that is merged thin sea ice thickness product (SMOS–SMAP) from Paţilea et al. (2019). However, Paţilea et al. (2019) pointed out that this retrieved ice thickness (or "apparent sea ice thickness" (Mchedlishvili et al., 2022) instead) is only valid under the assumption that the ice concentration is near-100% and has quite large uncertainties (up to 50 cm) in low concentration.

Sea ice production has been computed from hydrographic profiles in the Ross Sea (Thompson et al., 2020), or more commonly, using satellite-based techniques (Drucker et al., 2011; Ohshima et al., 2016; Tamura et al., 2016). However, to the best of our knowledge, no study quantified sea ice production in Southern Ocean open-ocean polynyas from observations. Sea ice production in coastal polynyas has also been studied using coupled models (Haid & Timmermann, 2013), especially the high-resolution ones that can simulate their formation and maintenance (Marsland & Wolff, 2001) and determine the relative contribution of each heat flux, including the radiative, turbulent and ocean heat ones (Wu et al., 2003). Similar studies have been conducted for the open-ocean polynyas, generally through coupled (Timmermann et al., 1999; Walkington & Willmott, 2006) and/or high-resolution climate models (Weijer et al., 2017; Kaufman et al., 2020). Weijer et al. (2017) in particular highlighted the enhanced sensible and latent heat fluxes over the open-ocean polynyas, which, in turn, have local impacts on precipitation, cloud characteristics, and radiative fluxes, using CESM at a synoptic-scale-resolving resolution (Small et al., 2014). Some of these modelling studies also quantify the heat transfer from the ocean to the atmosphere in Southern Ocean open-ocean polynyas (Campbell et al., 2019; Kaufman et al., 2020), but more often in coastal polynyas (Yao & Tang, 2003; Haid & Timmermann, 2013). Similarly, although the role of oceanic heat on sea ice production within coastal polynyas is already described in Guo et al. (2019), few studies, be it through observations of modelling, examine its influence on open-ocean polynyas.

Therefore, this study provides the first quantification of sea ice production in the Maud Rise open-ocean polynyas of 2016 and 2017, from observational data sets only, along with a critical analysis of the current methods and datasets available to compute sea ice production. The satellite retrievals and in-situ measurements that we use are described in Section 2, and the methods to calculate sea ice production within the polynyas as they develop are in Section 3. For the first time, when in-situ observations are available, we determine the upper oceanic heat flux within the polynya (Section 4.1). In Section 4.2, after computing the sea ice production, we investigate the local atmospheric and oceanic conditions that dominated the ice production in 2016 and 2017, respectively. We further explore the sensitivity and impacts of all input parameters that are related to the ice production calculation in Section 4.3. We then compare our results to other methods and those within coastal polynya and also address the other effects on the ice changes within the polynya in Section 5. Finally, a summary and conclusions and an outlook on future work are presented in Section 6.

2 Satellite, reanalysis, and in-situ data

2.1 Sea ice concentration from ASI

We focus on the region of Maud Rise within the Weddell Sea between 20°W and 20°E and from 75°S to 60°S, i.e., the area where open-ocean polynyas occasionally form (Heuzé et al., 2021). We use the daily ARTIST Sea Ice (ASI) Version 5 sea ice concentration (SIC) (Spreen et al., 2008; Melsheimer & Spreen, 2019) with a resolution of 6.25 km×6.25 km on a polar stereographic grid from the Advanced Microwave Scanning Radiometer 2 (AMSR2). We determine the extent of the 2016 and 2017 polynyas during the austral winter (May-October) by applying to these a standard 60% sea ice concentration threshold (Campbell et al., 2019), and "flood fill" algorithm to mask out the open ocean and the Antarctic continent, ice shelves, and adjacent coastal polynyas (Mohrmann et al., 2021). Fig. 1a shows the daily polynya area using this definition (lines) in 2016 (red) and 2017 (blue), but also the range of areas obtained when varying this threshold between 40 and 80% concentration (red/blue shading). It re-demonstrates that the open-ocean polynya detection does not depend on the threshold and that the open-ocean polynyas largely occurred in August and October 2016 and in September - October 2017, with a maximum extent over 100 000 km^2 during the 2017 event.

2.2 Radiative fluxes from CERES-SYN

As we explain in Section 3, we compute sea ice production via the energy budget. To quantify the radiative fluxes in the surface energy budget, we use solar and long-wave downwelling/upwelling surface fluxes from the Edition 4 Clouds and the Earth's Radiant Energy System (CERES) SYN1deg-Day (Doelling et al., 2013, 2016) dataset (hereafter referred to simply as CERES-SYN), which currently extends from 2002 until now. The data are computed from a radiative transfer model combining MODIS Terra, MODIS Aqua, and Geostationary imager satellites, meteorological profiles from the NASA Global Modeling and Assimilation Office (GMAO), and surface properties from several sources providing a global $1^\circ \times 1^\circ$ grid. To achieve the consistency between the computed and observed top of the atmosphere (TOA) fluxes from Terra and Aqua, small adjustments are made and then labelled as 'tuned' fluxes while the originally computed surface fluxes are 'untuned' (Rose et al., 2013). Despite its comparatively coarse resolution, CERES-SYN performs better than the reanalysis ERA5 in estimating radiative fluxes over the ocean surface (Tang et al., 2021). Here, we use the 'tuned' adjusted all-sky profile fluxes to quantify the energy budget in Section 4.2 and 'untuned' initial surface fluxes to carry out sensitivity studies in Section 4.3. All fluxes are interpolated to the ASI SIC spatial resolution.

2.3 Turbulent fluxes from reanalyses

To determine the turbulent flux in the energy budget, we use the method from L. Boisvert et al. (2020), described in Section 3.1; this method was previously applied to the satellite-based Atmospheric Infrared Sounder (AIRS) (Menzel et al., 2018). We here instead complement the ASI and CERES-SYN data with the 2 m air temperature, 1000 hPa air temperature, 1000 hPa relative humidity, 1000 hPa geopotential height, and 10 m wind speeds from a reanalysis instead of AIRS due to the missing/unknown values within the polynya region during thick cloud condition. In addition, the net radiative (longwave and shortwave) and turbulent (sensible heat: SH and latent heat: LH) fluxes from four different reanalyses are also used to quantify the consistencies and discrepancies between/among different reanalyses and methods proposed in our paper.

To decide which reanalysis to use for our region, we compared four reanalysis data sets to buoy measurements: ERA5 (Hersbach et al., 2020), the Japanese 55-year Reanalysis (JRA55) (Kobayashi et al., 2015), NCEP Climate Forecast System Version 2 (CFSv2) (Saha et al., 2014), and the Modern-Era Retrospective analysis for Research and Applications, version 2 (MERRA2) (Gelaro et al., 2017). The daily snow and automatic weather station buoy measurements (Nicolaus, Arndt, et al., 2017; Nicolaus, Hoppmann, et al., 2017) provide daily sea level pressure (SLP), 2 m

air temperature, and relative humidity that we compared to the reanalyses. We selected the buoys that had (1) been deployed in the Weddell Sea and (2) survived at least one austral winter (forty buoys in total, Fig. S1). Among the four reanalyses, JRA55 has the overall lowest bias and maximum correlation to all buoys (Fig. S2 to Fig. S4). Although ERA5 and MERRA2 also have low biases and high correlations for SLP (Fig. S2) and the 2 m air temperature (Fig. S3), JRA55 is the only reanalysis with a realistic relative humidity (Fig. S4). Therefore, for the rest of this manuscript, we use the daily atmospheric variables at a 1.25-degree resolution from JRA55. Note that investigating the reasons for the biases of each reanalysis would be beyond the scope of this paper.

2.4 Hydrographic data from SOCCOM floats

We also use hydrographic measurements from two Southern Ocean Carbon and Climate Observations and Modeling (SOCCOM) floats, with the WMOIDs 5904468 and 5904471, which fortuitously sampled the 2016 and 2017 open-ocean polynyas (see their trajectories in Fig. 1 (b) and (c)). The profiling floats measure with a 10-day cycle the temperature and salinity with an accuracy of $0.005°C$ and 0.01 psu, respectively, binned into 2 dbar intervals above 1000 dbar and 100 dbar intervals for levels between 1000 and 2000 dbar (Riser et al., 2018). From the individual SOCCOM profiles, we determine the mixed layer depth (MLD) using a potential density threshold $\Delta\sigma_\theta$ = 0.03 kg m^{-3} from the 10 dbar value (de Boyer Montégut et al., 2004; d'Ortenzio et al., 2005). Although this method is standard for the Southern Ocean, we investigate the sensitivity of our results to the use of another MLD calculation method in Section 4.3.

3 Methods

In this study, as has been done before for coastal polynyas (Tamura et al., 2008, 2011; Nakata et al., 2021), we determine sea ice production within the open-ocean polynyas via daily energy budgets. This section first describes the different terms of the energy budget, including the oceanic heat flux, and finishes with sea ice production and other methods for ice volume changes.

3.1 Energy balance within the polynya

Above the sea ice surface, the energy exchange between atmosphere, ice, and ocean is expressed as:

$$F_{net}^{top} = F_{SW} + F_{LW} + F_{SH} + F_{LH} + F_{TC} \tag{1}$$

where F_{net}, F_{SW} and F_{LW} are the net-, short- and longwave radiative fluxes, respectively, F_{SH} and F_{LH} are the sensible and the latent heat flux, and F_{TC} is the top surface conductive heat flux through the ice. Meanwhile, at the bottom of the ice, the balance is described as:

$$F_{net}^{bottom} = F_{OW} - F_{BC} \tag{2}$$

where F_{OW} is the oceanic heat flux into the ice and F_{BC} the basal conductive flux. Here, we assume that the conductive flux is continuous through the sea ice (West et al., 2019), which means that $F_{TC} = F_{BC}$ and the net flux used to produce/melt ice is either at the top or bottom. Thus, the net heat flux through the sea ice from the ocean to the atmosphere is further improved by combing Eq. 1 and Eq. 2 as:

$$F_{net} = F_{SW} + F_{LW} + F_{SH} + F_{LH} - F_{OW} \tag{3}$$

We now give more details about each term in dedicated subsections.

3.1.1 Turbulent flux

Satellite-based surface turbulent flux (F_{SH} and F_{LH}) retrievals rely on the bulk aerodynamic method (Monin-Obukhov similarity theory or MOST) (Panofsky, 1984) and an iterative calculation scheme (Launiainen & Vihma, 1990) following L. N. Boisvert et al. (2022), expressed as:

$$\begin{aligned} F_{LH} &= \rho\ S_r[C_{Ez,i}\ L_{e,i}\ SIC\ (q_{s,i} - q_z) + C_{Ez,w}\ L_{e,w}\ (1 - SIC)\ (q_{s,w} - q_z)] \\ F_{SH} &= c_p\ S_r[C_{Hz,i}\ SIC\ (T_{s,i} - T_z) + C_{Hz,w}\ (1 - SIC)\ (T_{s,w} - T_z)] \end{aligned} \tag{4}$$

where ρ is the air density, S_r the effective wind speed at 10 m that accounts for the enhancement of SH and LH fluxes by wind gustiness (and differs for stable and unstable boundary layers, (Taylor et al., 2018)), C_{Ez} (C_{Hz}) is the bulk water vapor (heat) transfer coefficient over ice (i) and water (w), $L_{e,i}$ ($L_{e,w}$) is the latent heat transfer of sublimation (vaporization) over ice (water), SIC is the sea ice concentration from ASI SIC, $q_{s,i}$ ($T_{s,i}$) is the saturation specific humidity (2 m air temperature) at the surface of the ice, $q_{s,w}$ ($T_{s,w}$) is the same but at the ocean surface, and q_z (T_z) is the air specific humidity (temperature) at 2 m, and c_p is the specific heat of air.

This method has regularly been applied for AIRS-based surface turbulent flux calculation (L. N. Boisvert et al., 2013, 2015; Monroe et al., 2021) with some modifications, including stable conditions and roughness lengths estimation of sea ice from Grachev et al. (2007); Andreas, Horst, et al. (2010); Andreas, Persson, et al. (2010). The 1000 hPa air temperature and specific humidity measured at different heights are consistently interpolated to a 2 m reference height based on the iterative process. Further considering the surface differences, the daily turbulent heat flux (LH and SH) are computed based on JRA55 and then interpolated for a 6.25 km×6.25 km pixel on a polar stereographic grid. The reader can find a more detailed description of the parameterization of these terms in L. N. Boisvert et al. (2013, 2015).

3.1.2 Oceanic heat flux

Similar to Ackley et al. (2020), the oceanic heat flux (F_{OW}) in Eq. 3 is calculated from the float data as (Maykut & McPhee, 1995):

$$F_{OW} = \rho_w c_w C_H u_{*0} \delta T, \tag{5}$$

where ρ_w = 1024 kg m^{-3} is the seawater density, c_w = 3980 J kg^{-1} K^{-1} the specific heat capacity of seawater, C_H = 0.0056 the heat transfer coefficient that can be used in the Weddell Sea (McPhee et al., 1999), u_{*0} the friction velocity at the ice/ocean interface, and $\delta T = T_{ML} - T_f(S_{ML})$ the deviation of the seawater temperature from the freezing point within the mixed layer. Here, $T_f(S_{ML})$ is defined as (Fujino et al., 1974): $-0.057\ S_{ML} + 1.710523\times10^{-3} S_{ML}^{3/2} - 2.154996\times10^{-4} S_{ML}^2 - 7.53\times10^{-4} P_{ML}$, where S_{ML} is the water salinity within the mixed layer in psu and P_{ML} is the pressure in decibars.

The magnitude of u_{*0} is obtained from the geostrophic drag relation as in Maykut and McPhee (1995):

$$\frac{|U_0|}{u_{*0}} = |\frac{1}{\kappa}[log(R_{o*} - A - iB)]|, \tag{6}$$

where $U_0 = U_{ice} - U_g$ is the vector describing the ice velocity U_{ice} relative to the surface geostrophic current in the ocean U_g, κ = 0.4 the von Karman's constant, and A and B the Rossby similarity constants. $R_{o*} = \frac{u_{*0}}{f z_0}$ is the surface friction Rossby number, where f is the Coriolis parameter and z_0 the roughness length for the under the ice surface. Based on Untersteiner et al. (2007), we use the constant values (A = 1.91, B = 2.12 and z_0 = 0.1m) obtained from the Arctic Ice Dynamics Joint Experiment (AIDJEX) stations measurements that have also been applied to the Weddell Sea (McPhee et al., 1999). Sea ice velocity (U_{ice}) is available from the NSIDC 25 km × 25 km daily sea ice drifting product through merging multiple passive microwave satellite and buoy observations (Tschudi et al., 2019). For the ocean geostrophic currents (U_g), we use the near-surface (0.50576 m depth) ocean current from the daily GLORYS (Global ocean reanalysis) 2V4 (Lellouche et al., 2013) in the Global Reanalysis multi-model Ensemble Product (GREP) product in 0.25°× 0.25° horizontal resolution.

3.2 Sea ice production estimation

In this study, we compute the daily frazil ice production rate as:

$$\frac{\partial hi}{\partial t} = \frac{-F_{net}}{\rho_{ice} L_{ice}}, \tag{7}$$

where F_{net} is computed as described in Eq. 3, ρ_{ice} is the ice density (= 920 kg m^{-3}), and L_{ice} = 279 KJ kg^{-1} the latent heat of fusion for ice production determined for the Ross Sea (Cheng et al., 2017), and which we assume can be applied to the Weddell Sea. Sea ice production within the polynya is then defined as the daily change within one grid cell (V_p):

$$V_p = \frac{-tA(1-SIC)F_{net}}{\rho_{ice}L_{ice}}, \tag{8}$$

where t (= 86,400 s) represents the seconds of one day, and A (= 6.25 km×6.25 km) is the area of a AMSR2 ice concentration grid cell. Earlier studies have used this algorithm to analyze ice production in coastal polynyas (Tamura et al., 2008, 2011; Nakata et al., 2021), but to the best of our knowledge, this study is the first to apply it to Southern Ocean open-ocean polynyas.

3.3 Sensitivity configuration

The computation of the produced sea ice volume V_p stems mainly from (1) the bulk parameter and threshold chosen in Eq. 8 and Eq. 5, (2) the radiative fluxes from CERES-SYN, and (3) the JRA55 atmospheric input. As acquiring the real uncertainties from the nonlinear heat flux calculation and the errors from the reanalysis data is near-impossible, we perform sensitivity tests to assess the relative changes in V_p when perturbing these parameters.

In Section 4.3, we, therefore, conduct the following perturbations on the sea ice, ocean, and atmospheric parameters:

- The sea ice concentration (SIC) threshold to detect a polynya, the sea ice latent heat of fusion (L_{ice}), the ice density (ρ_{ice}), and the ocean heat transfer coefficient (C_H) are perturbed by the upper and lower values from the references;
- We compute the mixed layer depth using the other five common algorithms: temperature threshold ($\Delta T = 0.2°C$), temperature gradient threshold ($\Delta\frac{\partial T}{\partial z}$ = 0.005^{o}C m^{-1}), intersection of the mixed layer and seasonal-thermocline fits (MLTFIT: $T_{MLfit} = T_{Thermfit}$), potential density gradient threshold ($\Delta\frac{\partial \sigma_\theta}{\partial z}$ = 0.0005kg m^{-4}), and potential-density fit ($\sigma\theta_{MLfit}$) from Holte and Talley (2009). We also quantify the effect of three choices of freezing temperature of sea water thresholds in -2.0^{o}C, -1.9^{o}C, and -1.8^{o}C, sea ice drifting error from NSIDC (Tschudi et al., 2019), and ocean surface current uncertainties from GLORYS multi-model ensembles (Garric & Parent, 2018);
- CERES-SYN 'tuned' data are replaced by 'untuned' data (see Section 2);
- and all JRA55 atmosphere parameters are perturbed within eight scenarios (±10, ±20, ±50, ±80%) of each value.

4 Results

4.1 Oceanic heat flux and net flux

Campbell et al. (2019) discussed deep overturning and upper ocean haline stratification in the Weddell Sea using the data from two SOCCOM floats that were sampled within the 2016 and 2017 polynyas. We here expand their study to compute the oceanic heat flux from the mixed layer within the polynyas using the same data set (Fig. 2, vertical dashed lines within the polynyas labelled with the ice concentration). As noted in Campbell et al. (2019), the mixed layer becomes shallower during the polynya events (white line, float 5904468 and 5904471 in Fig. 2a and c), probably as a result of ocean surface freshening from ice melt (Fig. 2b and d). Meanwhile, ocean temperatures both below and within the mixed layer are above freezing while the polynya is open (positive values on Fig. 2a and c, most clearly visible during the 2017 polynya).

Although the apparent sea ice thickness from SMOS-SMAP (purple line) decreases at the location of the floats during the polynyas, the oceanic heat flux F_{OW} (green lines), calculated from the floats and Eq. 5, is not statistical significantly different in the presence and absence of a polynya. The average oceanic heat flux along the float trajectory for the period during which sea ice con-

centration is lower than 60% is 36.08 Wm^{-2} during the 2016 polynya, and 30.72 Wm^{-2} during the 2017 polynya in Table 1. By combining the two floats measurements, the monthly mean oceanic heat flux is thus presented in Table 1 within 2016 and 2017, with the maximum being about 67.28 and 52.26 Wm^{-2}, respectively. These values are close to that from A. L. Gordon and Huber (1990) (41 Wm^{-2}) but larger than the annual mean oceanic heat flux in Petit and Norro (2000) (see their Fig. 15), although none of these was measured in a polynya; the discrepancy will nonetheless be addressed later in this manuscript.

Through the floats measurements, the ocean heat flux is estimated every ten days. Therefore, the daily ocean flux is acquired through linear interpolation between the successive two (10-day resolution) float values for each float. And then, the mean daily ocean flux (thick light green lines in Fig.2b and d) is averaged from float 5904468 and 5904471. Here, the daily resolution average heat energy from the ocean is included in the daily net heat flux in the 2016 and 2017 polynya energy budget, subtracting them as in Eq. 3, and denoted as "F + O" in the following analysis. As described in Section 3, F + O includes the radiative flux retrieved from CERES-SYN, the turbulent flux computed from the MOST method with JRA55 input, and the float-based oceanic heat flux. Fig. 3 contrasts "our" (F + O) net flux within the 2016 and 2017 Maud Rise polynyas to the one from JRA55. Generally, the net flux is negative, i.e., the ocean loses heat to the atmosphere, which is to be expected when sea ice is thin or open. In particular, in 2016 (Fig. 3a), F + O shows an extreme heat loss (over 300 Wm^{-2}) from the ocean near the end of July, when the polynya is opening. The heat flux mainly remained negative during the entire polynya event. The larger 2017 polynya (Fig. 3b) had several positive heat intrusions into the ocean, which would melt the ice. Especially by the end of September, all computations agree to reveal a positive net flux of 25 Wm^{-2}, by the ocean losing over 350 Wm^{-2} heat before the polynya reaches its maximum on 23-Sep.

The flux changes are consistent among all data sets. In fact, the computed net fluxes are significantly correlated with each other (Table S1). Table S1 also compares the net flux calculation from F + O but with the other three reanalyses input, denoted as F + O (ERA5, CFSv2, MERRA2) in the following. Due to the lack of partial sea-ice cover in the grid cells used by JRA55 (Kobayashi et al., 2015; Tsujino et al., 2018), those from F + O and JRA55 have the lowest correlation compared to others. The 0 or 100% sea ice treatment in JRA55 also explains that the spatial variability of net flux is the smallest in JRA55 during the freezing seasons, while the temporal variability is the largest in F + O. However, high correlations (>0.85), which are between direct flux from the reanalyses and those from F + O feeding in those reanalyses, e.g., between ERA5 and F + O (ERA5), prove the robustness of the F + O algorithms.

To summarise, we computed the upper ocean heat flux when the open-ocean polynya occurred based on the floats measurements. Then, for the first time, the net flux proposed here, F + O, also incorporates this observationally-deduced flux in the heat budget over the Maud Rise open-ocean polynya. We now use this heat budget to examine the sea ice production within the latest two Maud Rise polynyas.

4.2 Sea ice production in the polynyas, and the role of the atmosphere and ocean

Using the net flux estimated from F + O, we compute the daily sea ice production through Eq. 7. Fig. 4a and b show the daily ice produced within the day of maximum polynya extent in 2016 and 2017 (the same two days as in Fig. 1). Average (maximum) sea ice produced on 8-Aug-2016 is about 0.073 m (0.149 m) and reaches 0.097 m (0.179 m) on 23-Sep-2017. Note for both years the region-dependent distribution, in which the production is more prominent in the northern part of the polynya in response to the sensible flux from the ocean (not shown).

The monthly distribution and the related statistical parameters of sea ice production for each cell within the 2016 (2017) polynya are shaded in red (blue) in Fig. 4c. The peak production for 2016 is in July, with 1.8×10^{-3} km^3/day on average. In 2017, although the polynya has a large extent throughout October, the amount of ice produced is highest in September while the polynya grows, corresponding to the September significant heat loss (Fig. 3). The average September 2017

sea ice production for each 6.25 km×6.25 km cell is over 2.5×10^{-3} km^3/day, with over 70% among them over 2.0×10^{-3} km^3/day. There are also negative ice production (melting) values over the wider Maud Rise (within the polynya area), mainly in May before the seasonal ice cover has fully settled and in (late) October as the sunlight returns. Note that the dynamics aspect is comparatively small and cannot explain these values, as we will show in Section 5. Finally, the accumulated ice produced during the freezing season (May to October) is summarized in Table 2: 80.11 km^3 in 2016 and 197.86 km^3 in 2017 in total within the polynyas. As we will discuss later in this manuscript, this is the same order of magnitude as produced by the largest coastal polynyas.

We further examine the relationship between daily sea ice production, near-surface atmosphere condition from JRA55, and ocean current from GLORYS to find the determining factors for the variation of V_p (Table 2) in 2016 and 2017. As expected, we find that the sea ice production V_p is highly correlated with the polynya extent S_p, especially in 2016 (correlation coefficient of 0.64). The volume V_p is also negatively correlated with the 2 m air temperature (T), especially in 2017 (-0.51), and those anti-correlations dominate the north of the Maud Rise region (Fig. S5a). That is, as expected, a cold atmosphere is associated with large ice production. There is also a slight positive correlation (Fig. S5b) between the volume of ice produced and the 10 m wind speed ($|U_{\text{wind}}|$) for both years, probably because the turbulent heat flux to the atmosphere is determined by T and $|U_{\text{wind}}|$. Correlations between ice production and ocean surface currents ($|U_{\text{ocean}}|$), although significant, are very small, especially in 2017 (0.08). Note that there are large uncertainties in the time series of these potential drivers, not least due to the differences in spatial resolutions, so it is no surprise that the dominating causality cannot be established. In addition, taking the dependent relationship between $|U_{\text{wind}}|$ and $|U_{\text{ocean}}|$ into account, we perform two multiple linear regression analyses in which V_p is taken as a variable explained by (1) T and $|U_{\text{wind}}|$, (2) T and $|U_{\text{ocean}}|$, respectively (Table 2). We find again that T is the dominant factor that determines V_p in the open-ocean polynyas while $|U_{\text{ocean}}|$ has the least influence. Interestingly, the contributions differ between the 2016 and 2017 polynyas; The wind influence on V_p is larger within the relatively small 2016 polynya, while the 2 m air temperature clearly dominates in the large 2017 polynya. Lastly, we find that unlike ice production within coastal polynyas (Nihashi & Ohshima, 2015; Nakata et al., 2021), geostrophic winds exert a negligible influence (not shown) on the 2016/2017 open-ocean polynyas.

4.3 Sensitivity study

As introduced in Section 3.3, we acknowledge that all parameters involved in the sea ice volume computation have inherent uncertainties that impact our results, but these uncertainties, unfortunately, cannot be obtained directly. We, therefore, instead quantify the sensitivity of V_p for the 2016 and 2017 open-ocean polynyas to perturbations of all the bulk, sea ice, oceanic, and atmospheric parameters (Table 3, Table S2 and Fig. S6). When possible, to clarify, Table 3 also gives α, the ratio of relative changes in V_p to those in the input value.

The bulk ice parameters are varied within the ranges found in the literature (see Table 3). These include the sea ice concentration threshold for polynya determination, L_{ice}, ρ_{ice}, and C_H. Among them, the SIC threshold for polynya determination exerts the largest impact on sea ice production, with the α being over 1. This is no surprise given the results of the previous section: a different threshold changes the detected area of the polynya, which we found to be strongly correlated to V_p.

For the sensitivity to the oceanic terms, we notably recompute the mixed layer depth using the other algorithms/thresholds used in the literature, as well as different values for the freezing point of sea water, commonly used instead of the actual salinity and pressure-dependent value. We also quantify the sensitivity to the NSIDC ice drift and GLORYS ocean currents. We find that among these, the MLD algorithm has the largest impact (Table 3): nearly 40% of the ice production in 2017 (Table S2) is reduced if the MLD comes from the MLFIT algorithm, i.e. is computed as the intersection between the MLD and thermocline (Holte & Talley, 2009). The MLFIT algorithm suggests the average MLD is 28.2 m deeper in 2017, corresponding to over 70%

extra heat storage in the upper ocean. However, Holte and Talley (2009) showed that this method might misidentify the thermocline from the polar profile for the polar regions. Overall, compared to the potential density threshold, the gradient threshold algorithms for both temperature and density always obtain a larger ice production, while those based on the fit algorithm tend to produce significantly less ice.

The sensitivities from all atmospheric parameters are considered through changing into 'untuned' CERES-SYN data or proportionally increasing/decreasing the JRA55 input. The sensitivity results show that the most substantial impact arises from the temperature at 1000 hPa (α of 1.43 to 3.40). That is, 1% of temperature changes can at least result in 1.4% of ice production variation (see, e.g. 2016 on Fig. S6). This is no surprise considering that in the previous paragraph, we found that sea ice production was most strongly correlated to near-surface air temperature.

Generally, the most dominant factor for ice production is near-surface (1000 hPa) temperature, followed by polynya threshold, mixed layer depth definition, the latent heat of fusion, and 2 m temperature.

5 Discussion

5.1 Comparison of the methods for sea ice production

The method we used here to compute sea ice production is the most commonly used for Antarctic coastal polynyas, but it is not the only method. Sea ice production can also be estimated from the "freezing degree days" (FDD) or simply by comparing day-to-day changes in SMOS-SMAP thin ice thickness, although large uncertainties (Ludwig et al., 2019; Macdonald et al., 2022), see Text S1. Here, we will use the term apparent 'sea ice change' (V_{apparent}) instead of 'sea ice production' for the above FDD and SMOS-SMAP methods for less ambiguity. Preußer et al. (2019) pointed out that flux-deduced sea ice production, e.g. F + O, is typically regarded as a potential upper limit for thermodynamically induced ice changes.

We compare these three methods in Fig. S7: red and blue shadings are from our F + O estimation, identical to Fig. 4; purple lines are for the FDD sea ice and green light for the SMOS-SMAP one. Sea ice changes from SMOS-SMAP are much smaller than from the other two methods, with monthly means hardly above 0 even in 2017. The result is the same when accumulated over the entire May-October season (second column in Table 2 and dotted shadings and circle lines in Fig. 5): V_{apparent} from SMOS-SMAP (square bracket, left) is only 19.5 km^3 in 2017, while that derived from FDD (square bracket, right) and F + O (no bracket) are comparable, over 50 km^3 in 2016 and over 180 km^3 in 2017. This result can partly be explained by the definition of these two auxiliary methods. The FDD estimation constantly accumulates values. Thus the daily V_{apparent} is always positive, i.e. ice can only grow with this method. In contrast, most of the SMOS-SMAP V_{apparent} is negative, indicating half of the sea ice melts during the occurrence of the polynya, which is in agreement with the oscillations in heat fluxes from Fig. 3. Considerable uncertainties exist in the SMOS-SMAP product (Paţilea et al., 2019), up to 30 cm. Its current retrievability limit of 50 cm also hampers its use for sea ice volume change studies. Therefore, although the consistency between potential ice production and actual sea ice changes cannot be definitely verified, our results provide an uppermost limitation of ice production, which can impact the sea ice budget in general.

5.2 Comparison of the Maud Rise sea ice production to that of Antarctic coastal polynyas

Although open-ocean polynyas rarely occur in the Southern Ocean, we find that the ice production within them is comparable to or even more extensive than that in coastal polynyas. Fig. 5 compares sea ice production among the 13 major Antarctic coastal polynyas computed by (1) Nihashi and Ohshima (2015) (yellow patches, see their Table 1, average over 2003-2010) and (2) Tamura et al. (2016) (yellow circles, see their Table 1, average over 1992-2013) to that from our F + O

(red and blue patches). The differences between the Nihashi and Ohshima (2015) and Tamura et al. (2016) estimate result from different methods, data sets and spatial coverage. The most considerable contrast (271 v.s. 38 km^3) is over the Weddell Sea (W), where Tamura et al. (2016) integrated ice production in coastal polynyas along an extensive stretch of coastline, while most of them are labelled as fast ice and hence excluded by Nihashi and Ohshima (2015). There, an extra estimation of 155 km^3 from 1992 to 1998 is provided by Renfrew et al. (2002).

There is more agreement at the other coastal polynya locations (Fig. 5), highlighting that the Ross Ice Shelf (R) polynya is the largest producer (over 300 km^3 sea ice from March to October). We find that the second-largest is the 2017 Maud Rise open-ocean polynya (197.86 km^3), ahead of the Cape Darnley (CD: ~158 km^3) and Mertz (M: ~152 km^3) coastal polynyas. Although lower, the sea ice production in the 2016 Maud Rise polynya is nonetheless the 8th highest (80.11 km^3). Therefore, a sizeable open-ocean polynya can lead to extensive ice production that is comparable to or even larger than the coastal polynya "ice factories".

High ice production in a coastal polynya can produce dense shelf water (DSW) that contributes to AABW formation (Ohshima et al., 2016). For example, polynyas in Ross Ice Shelf and Terra Nova Bay are taken as the drivers for Ross Sea Bottom Water (Fusco et al., 2009; Comiso et al., 2011); sea ice production in the Cape Darnley polynya is directly linked to very saline DSW (>34.8) (Roquet et al., 2013), and the primary DSW source of Cape Darnley bottom water (CDBW) (Ohshima et al., 2013), and the Mertz polynya is identified as the source of Adélie Land Bottom Water (Williams et al., 2008). Therefore, such a large ice production and brine rejection in the open ocean would significantly impact the local stratification and potentially lead to dense water formation (Kusahara et al., 2017), although, e.g. Campbell et al. (2019) found no indication of deep convection following the 2016 and 2017 polynyas.

5.3 Dynamics inside the polynya

Another significant contributor to the sea ice budget in the polynya is the sea ice motion. Sea ice convergence from outside of the polynya to the polynya causes a net ice gain for the polynya, while ice divergence out of the polynya causes a net ice loss. Several studies compared the contribution of the dynamic and thermodynamic processes changing sea ice area in the Weddell Sea (Holland & Kwok, 2012; von Albedyll et al., 2022). In particular, based on a concentration budget analysis, Holland and Kwok (2012) found that during a typical freezing season, sea ice concentration over Maud Rise (named King Håkon Sea in their paper) is mainly controlled by thermodynamic component. Huot et al. (2021) found a similar result in the polynya in their 5 km sea ice-ocean model. Besides, unlike coastal polynyas that are controlled by dynamic processes (katabatic wind, latent heat), open-ocean polynyas are dominated by sensible fluxes, i.e. thermodynamics. Finally, the insignificant correlation between V_p and geostrophic wind, which is correlated with the ice motion, in Section 4.2 also supports the hypothesis of a minor impact from the dynamics.

Nonetheless, we quantify the relative contributions from thermodynamic and dynamic processes in the ice production/volume changes with the development of the 2017 Maud Rise open-ocean polynyas. We here show only the period September-October 2017 (49 days in total), which exhibited the largest changes in sea ice production and polynya area. Here, in a very simple case, we focus on the sea ice horizontal transport/advection and consider the "free drift" condition in which the rheology term, ridging redistribution, and internal force are neglected. See more computation details in Text S2 and Fig. S8. We find that the 49 days of accumulated daily ice volume changes due to ice advection computed from the NSIDC sea ice drift data (~ 5.6 km^3) is only 30% of the total sea ice volume change over the same period (~ 18.5 km^3). This estimation is but an approximation, owing to the low resolution of the sea ice drift dataset, e.g. 25 km×25 km NSIDC products used here. We expect that the new daily sea ice velocity data sets from the proposed "swath-to-swath" algorithm (Lavergne et al., 2021), combined with more accurate sea ice thickness retrievals from satellites, will reduce the uncertainty of that estimation.

5.4 Discussion of the oceanic heat flux estimation

As explained, e.g. in Guo et al. (2019), sea ice production in open-ocean polynyas is reduced by the upwelling of oceanic heat flux from the comparatively warm, modified Circumpolar Deep Water (CDW). We here estimated the oceanic heat flux from direct observations collected by drifting profilers. Noted that within the sea ice energy budget, the ocean heat effects are within the mixed layer (up to 200 m in Fig. 2). Previous studies have found that the average upper-ocean heat flux in the western Weddell Sea varies from 7 W m^{-2} (Lytle & Ackley, 1996) to 41 W m^{-2} (A. L. Gordon & Huber, 1990) during autumn and early winter.

Over Maud Rise, in particular, McPhee et al. (1999) found about 23 W m^{-2} during the ANZFLUX crewed drift in 1994. Our maximum (and average) estimations from the float measurements collected during the 2016 and 2017 polynyas (within 60% threshold in Table 1), 58.9 (36.1) W m^{-2} and 66.6 (30.7) W m^{-2}, reveal that the oceanic heat flux during a polynya is high compared to the previously observed values. To the best of our knowledge, this is the first estimation of the upper oceanic flux before and during the recent Maud Rise polynyas. Admittedly, the parameterizations/choices of the above bulk values in Eq. 6 require more idealized laboratory experiments and actual field works to better represent the current Weddell Sea or Antarctic research. The largest uncertainty comes from the measurement method itself though: be it from a mooring, a ship, or a float, all oceanic observations are single profiles. Our results and that of others, e.g. Mohrmann et al. (2022) show in contrast a large spatial variability over the polynya region and a daily (or higher) temporal variability. We need observations at a high spatio-temporal resolution, for example from a flotilla of floats sampling daily, to resolve these scales of variability in the polynya, and more accurately quantify the contribution of the ocean through its life cycle.

6 Conclusions

We estimate sea ice production within the 2016/2017 large Maud Rise open-ocean polynyas from the sea ice surface energy budget computed from the CERES-SYN satellite product and JRA55 atmosphere reanalysis. We show that this thermodynamics contribution dominates ice growth and production. For the first time, we also incorporate the oceanic flux into the heat balance, which is evaluated from direct observations collected by drifted profilers. This oceanic heat flux is 36.08 (30.72) Wm^{-2} within the 2016 (2017) open-ocean polynya, on average.

We find large ice volumes of ice produced in these two polynyas, especially in September 2017, when the open-ocean polynya was large. We find that the accumulated volume of 2017, 198 km^3, is the second-largest compared to 13 main Antarctic coastal polynyas (Fig 5). Consistent with the formation mechanism of open-ocean/sensible heat polynya, we find that the daily ice production is most correlated to the 2 m air temperature but only weakly correlated to winds, further showing that these polynya events are primarily thermodynamically controlled. In addition, we found significant sensitivities of the sea ice volume calculation to the 1000 hPa air temperature, the sea ice concentration threshold for polynya definition, and the mixed layer depth computation. These could explain why polynyas are so poorly represented in climate models (Mohrmann et al., 2021): the atmosphere, sea ice, and ocean diagnostics need to be accurate simultaneously. Our results suggest that the rarely-occurring but extensive open-ocean polynya can result in substantial ice production, which is closely related to open-ocean deep convection, another process that is poorly represented in current climate models (Heuzé, 2021). High-resolution models perform better (Kaufman et al., 2020), but modelling and observation studies, including this one, remain limited as lateral, and bottom ice melting cannot be directly estimated from the heat flux (Nihashi et al., 2012). These atmosphere - ice - ocean interactions and their variability in polynyas urgently need to be better understood and disentangled, especially for deep ocean ventilation, AABW formation, and carbon sequestration (Bernardello et al., 2014) given the increasingly vital role of polar processes on the global climate system.

Still, more in-situ observations and model studies need to be combined to explain (1) the detailed feedback between the ocean, ice, and air above polynyas; (2) how ice production responds to the pan-Antarctic open-ocean polynya and influences the local atmosphere circulation and deep convection; and (3) how polynya heat loss influences local/high-latitude climate variability. Fortunately, more specifically-designed satellites such as the Ice, Cloud, and Land Elevation Satellite (ICESat)–second-generation ICESat (ICESat-2) (Xu et al., 2021) and the second Cryosphere Satellite (CryoSat-2) (Kacimi & Kwok, 2020) are coming. They will allow for a more realistic detection of sea ice distributions and even snow cover parameters and help to answer the far-reaching consequences of extensive open-ocean polynya activity for the global ocean circulation and ice sheet mass balance with climate change.

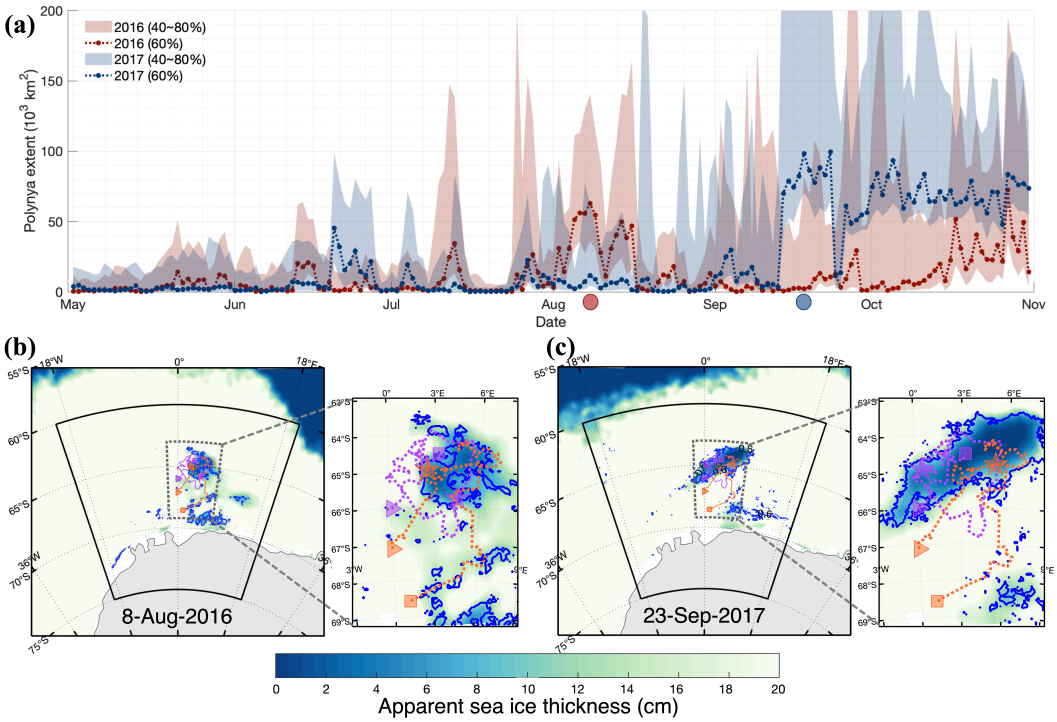

Figure 1. (a) Daily extent (in 10^3 km^2) of the polynya in 2016 (red) and 2017 (blue) based on the 60% sea ice concentration threshold (dashed lines) and within the range of 40 and 80% thresholds during the period from May to October within the wider Maud Rise region (solid lines outlined in (b) and (c)). (b) and (c) are apparent sea ice thickness from SMOS-SMAP (shadings) at the largest polynya extent day of each event on 8-Aug-2016 and 23-Sep-2017, respectively. Their dates are denoted with circles in (a). Orange (purple) dots are the trajectory of profiling float 5904468 (5904471) (triangle: starting on 19-Jan-2015 and 12-Dec-2014; square: ending on 14-Oct-2019 and 7-Jun-2019), identical on both panels, while the stars indicate the float location on 8-Aug-2016 and 23-Sep-2017. Right corner inset figures: zoom in the dashed lines region.

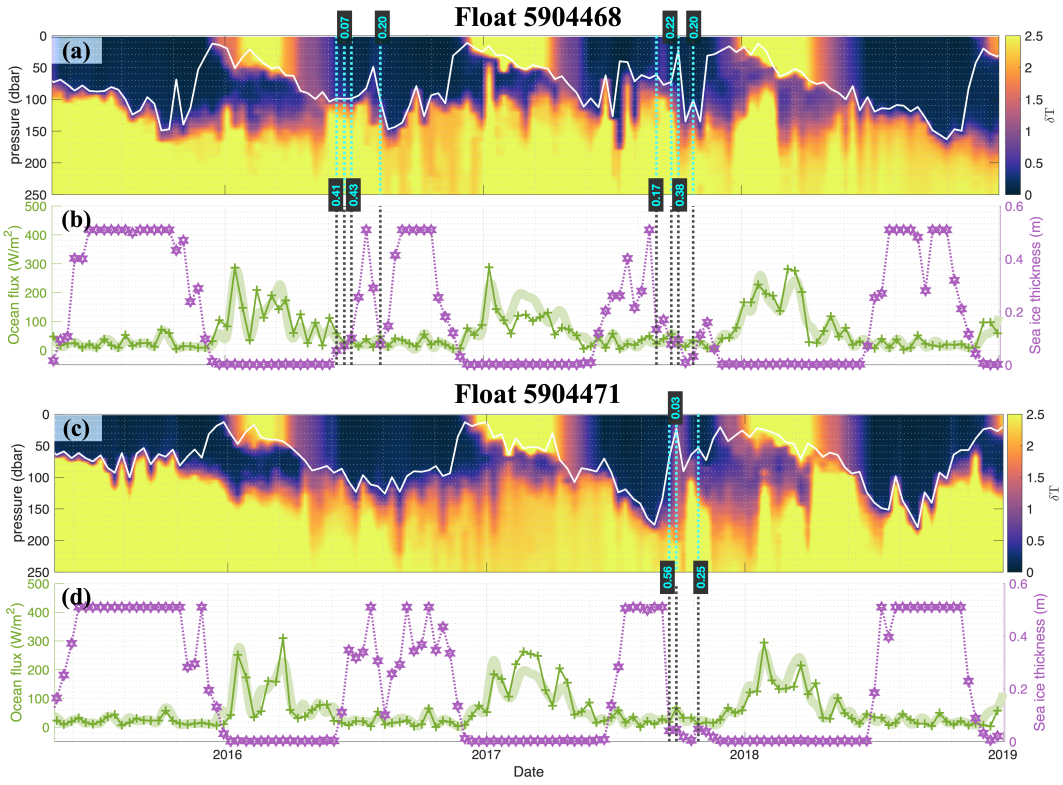

Figure 2. Time-depth sections from the profiling float 5904468 and 5904471: (a) and (c), temperature difference (δT, Units:°C) between the measured temperature and the freezing temperature of seawater (shading), mixed layer depth (MLD, white line), and sea ice concentration value from ASI SIC during the polynya (vertical dashed cyan line); (b) and (d), sea ice thickness (purple) and oceanic heat flux calculated from Eq.5 (thin green). Thick light green lines are the mean daily ocean heat flux from float 5904468 and 5904471.

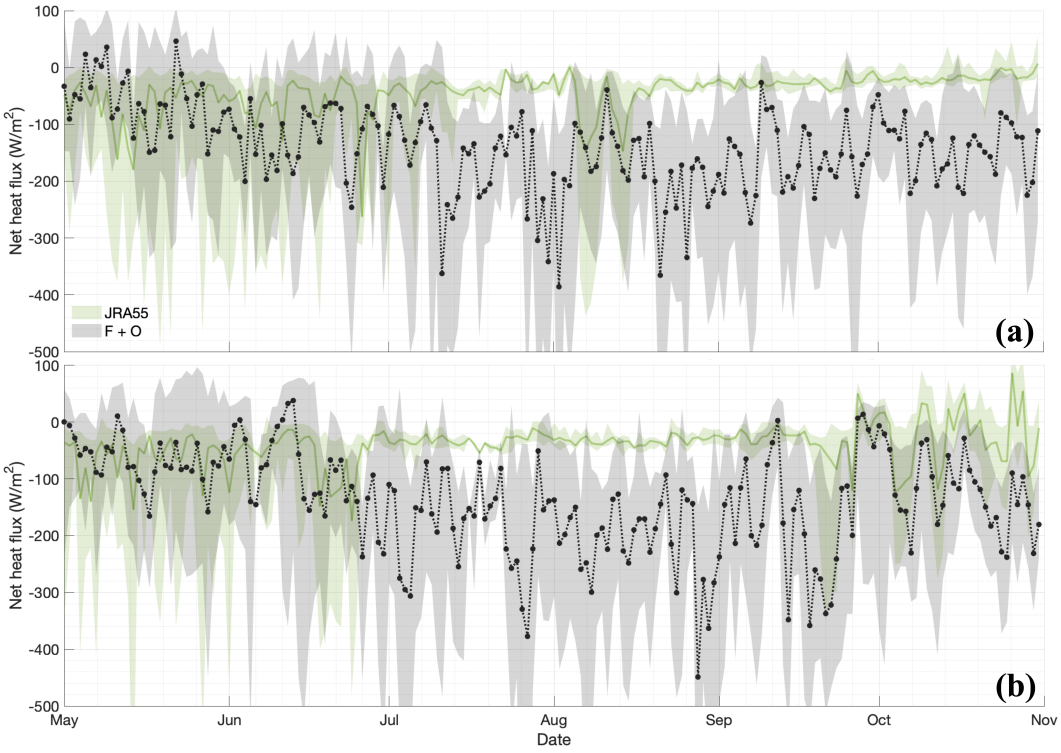

Figure 3. Daily upward net heat flux (Units: W m^{-2}) from JRA55 (light green) and from Eq. 3 (grey), within the 2016 (a) and 2017 (b) Maud Rise polynyas (60% concentration threshold) during the freezing seasons (May to October). The shadings indicate the 1% to 99% percentiles, and solid, and dashed lines are the mean flux value within the polynyas.

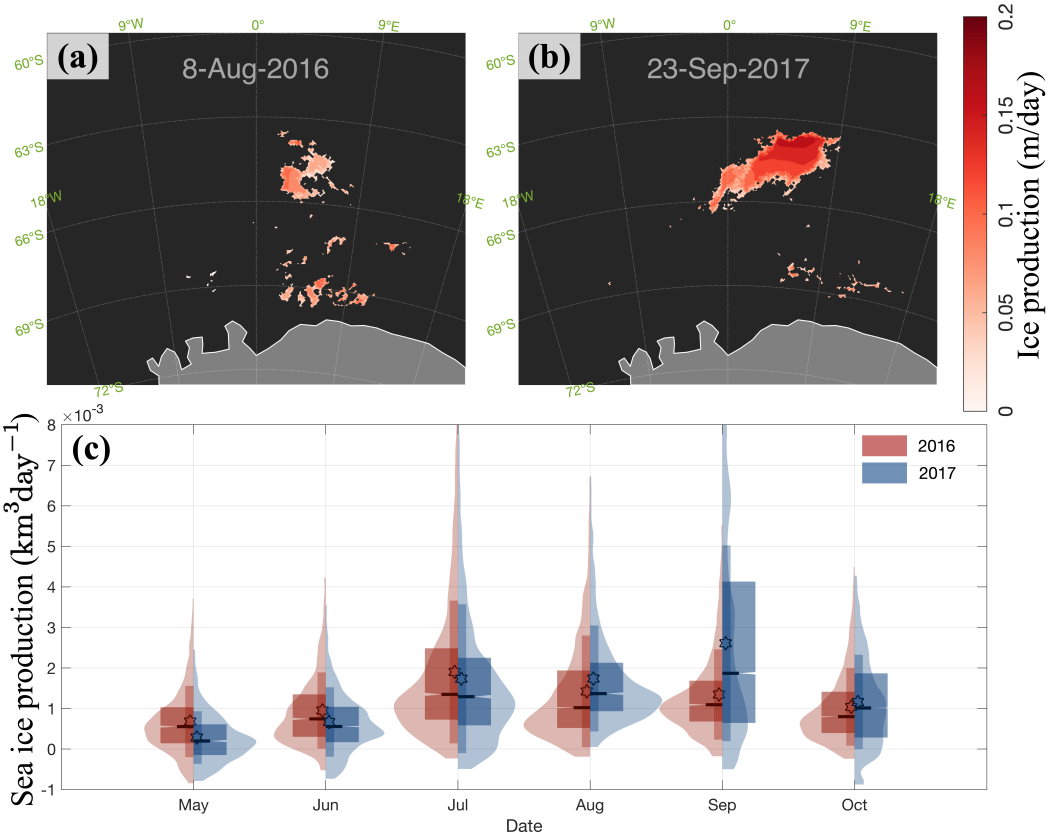

Figure 4. Spatial distribution of sea ice production on (a) 8-Aug-2016 and (b) 23-Sep-2017, i.e. days of maximum polynya extent for each year (same days as in Fig. 1).(c) Distribution of monthly sea ice production (Units: km^3 day^{-1}) from Eq. 7 within the 2016 (red, left) and 2017 (blue, right) Maud Rise polynyas. The violin shadings cover the range of 1st and 99th percentiles, the upper (lower) boundaries of slim boxes are the mean +(-) standard deviation, while the upper (lower) ones in thick boxes are the 3rd and 1st quartiles of ice production. The stars (short-solid horizontal lines) represent the mean (median) of monthly production.

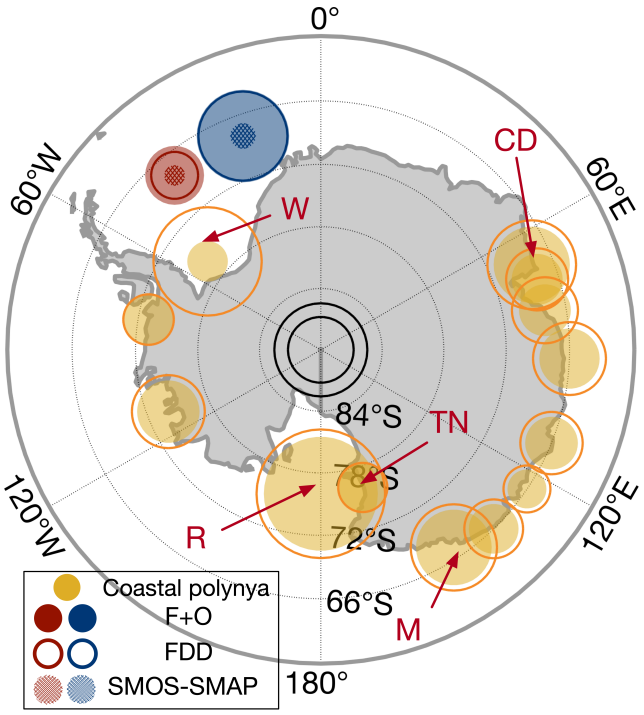

Figure 5. May-Oct accumulated polynya ice production within the Maud Rise region in 2016 (red) and 2017 (blue) from all three methods; "F + O" in plain circles, "FDD" in solid circles lines and "SMOS-SMAP" in dotted areas. The yellow patches represent the mean coastal polynya ice production between 2003 and 2010 (March to October) from Nihashi and Ohshima (2015) Table 1, while the yellow circle lines are the estimation between 1992 and 2013 from Tamura et al. (2016) Table 1. The centred small (large) white circle corresponds to 100 (200) km^3 ice production. (W for Weddell Sea, CD for Cape Darnley, M for Mertz, TN for Terra Nova Bay, and R for Ross Ice shelf).

Table 1. Mean ocean mean flux (Units: W m^{-2}) from float observations during the winter months and within the 60% ice concentration regions, denoted in Fig. 2.

Years	May	Jun	Jul	Aug	Sep	Oct	Within 60% threshold
2016	67.28	27.17	23.62	24.18	18.90	30.00	36.08
2017	52.26	23.55	32.37	22.87	41.13	23.78	30.72

Table 2. 2nd column: accumulated polynya ice production (V_p) during the freezing seasons (May to October) within the key region, while the italic values in the brackets represent the V_{apparent} estimation from "SMOS-SMAP" (left) and "FDD" (right). 3th-6th columns: correlation coefficient between the daily May-October ice production V_p and polynya extent (S_p), 2 m air temperature (T), 10 m wind speed ($|U_{\text{wind}}|$) from JRA55, ocean surface current ($|U_{\text{ocean}}|$) from GLORYS, respectively. 7th-10th columns: standardized partial regression coefficients (β_T, $\beta_{|U_{\text{wind}}|}$, γ_T, $\gamma_{|U_{\text{ocean}}|}$) from two multiple linear regression analysis consisting of (1) T and $|U_{\text{wind}}|$, (2) T and $|U_{\text{ocean}}|$. All of the values are significant at the 99% confidence level.

Years	Winter ice production (km^3)	V_p $v.s.$ S_p	V_p $v.s.$ T	V_p $v.s.$ $\|U_{\text{wind}}\|$	V_p $v.s.$ $\|U_{\text{ocean}}\|$	β_T	$\beta_{\|U_{\text{wind}}\|}$	γ_T	$\gamma_{\|U_{\text{ocean}}\|}$
2016	80.11 *[15.61,51.13]*	0.64	-0.36	0.26	0.10	-0.41	0.36	-0.36	0.20
2017	197.86 *[19.53, 183.74]*	0.37	-0.51	0.10	0.08	-0.50	0.25	-0.46	0.11

Table 3. Sensitivities in accumulated May–October polynya sea ice production in 2016 and 2017 to the input data, including sea ice concentration (SIC) threshold, sea ice latent heat of fusion (L_{ice}), sea ice density (ρ_{ice}), ocean heat transfer coefficient (C_H), the other five algorithms for mixed layer depth definition ($\Delta T = 0.2°C$; $\Delta\frac{\partial T}{\partial z} = 0.005^oC\ m^{-1}$; $\Delta\frac{\partial \sigma_\theta}{\partial z} = 0.0005 kg\ m^{-4}$; $T_{MLfit} = T_{Thermfit}$; $\sigma\theta_{MLfit}$), freezing temperature of sea water, NSIDC sea ice drift, GLORYS ocean current, radiative flux from 'untuned' CERES-SYN, and five atmospheric variables from JRA55. The slash's left and right sides are each input's lower and upper perturbation. The respective production changes for 2016 and 2017 polynyas are shown in brackets. The literature in which they were used is also cited. When meaningful, α is the ratio of V_p changes (Units: %) over the perturbed changes (Units: %).

Variable	Perturbed value	V_p change (%)	α
SIC (%)	50 (Campbell et al., 2019) / 70 (Parmiggiani, 2011)	-19.0 / 21.2	1.14~1.27
L_{ice} (J kg^{-1})	276 (Yu & Rothrock, 1996) / 334 (Nihashi & Ohshima, 2015)	1.1 / -16.5	0.83~1.01
ρ_{ice} (kg m^{-3})	900 (Tamura et al., 2008) / 950 (Jardon et al., 2014)	2.2 / -3.2	≈1.0
C_H	0.005 / 0.006 (McPhee, 1992)	[5.82,3.52] / [-3.9,-2.35]	0.33~0.55
Mixed layer depth+ (m)	ΔT; $\Delta\frac{\partial T}{\partial z}$; $\Delta\frac{\partial \sigma_\theta}{\partial z}$; $T_{MLfit} = T_{Thermfit}$; $\sigma\theta_{MLfit}$ (Holte & Talley, 2009)	-39.10~6.37	-
Freezing temperature of sea water+ (^oC)	-2.0(Thurman, 2002); -1.9(Wetzel et al., 2004); -1.8(Hunke et al., 2017)	-4.32~7.6	-
NSIDC sea ice drift+ (m s^{-1})	Error variance (Tschudi et al., 2019)	-8.8~1.69	-
GLORYS ocean current+ (m s^{-1})	Multi-model ensemble uncertainties (Garric & Parent, 2018)	-1.54~2.03	-
CERES-SYN	'untuned'	[-0.73,1.94]	-
T_{2m} (^oC)	-80, -50, -20, -10/10, 20, 50, 80%*	3.58~85.68 / -65.20~-3.46	0.31~1.07
$T_{1000\ hPa}$ (^oC)		-172.36~-16.51 / 16.75~271.91	1.43~3.40
Geopotential height (m)		0.23~5.81 / -1.49~-0.19	0.01~0.07
Relative humidity (%)		3.23~31.69 / -30.66~-3.23	0.32~0.40
Wind speed (m s^{-1})		-81.14~-6.92 / 6.85~73.82	0.65~1.01

+Detailed ice production changes (Units: %) for each parameter perturbation can be found in Table S2.
*Detailed ice production changes (Units: %) for each parameter can be found in Fig. S6.

7 Open Research

The ASI AMSR2 sea ice concentration datasets (Spreen et al., 2008; Melsheimer & Spreen, 2019) are available from Bremen University data center: `https://seaice.uni-bremen.de/data`. The measurements from the two profiling floats were downloaded from the SOCCOM quality-controlled archive (Johnson et al., 2017): `http://library.ucsd.edu/dc/collection/bb4473712z`. The sea ice thickness from SMOS (Huntemann et al., 2014) and SMOS-SMAP (Paţilea et al., 2019) is provided by Bremen University at: `https://seaice.uni-bremen.de/databrowser/`. ERA5 reanalysis data are from the European Centre for Medium Range Weather Forecast (ECMWF), available via: `https://cds.climate.copernicus.eu/cdsapp#!/dataset/reanalysis-era5-single-levels`. The hourly Modern-Era Retrospective analysis for Research and Applications version 2 (MERRA-2) datasets are available via: `https://goldsmr4.gesdisc.eosdis.nasa.gov/data/MERRA2/M2T1NXSLV.5.12.4/` The 3-hourly Japanese 55-year Reanalysis (JRA55) are available via: `https://rda.ucar.edu/datasets/ds628.0/` The hourly NCEP Climate Forecast System Version 2 (CFSv2) are available via: `https://rda.ucar.edu/datasets/ds094.1/` The radiative fluxes datasets from CERES and GEO-Enhanced TOA, Within-Atmosphere and Surface Fluxes, Clouds and Aerosols Daily Terra-Aqua Edition4A [CER_SYN1DEG-DAY_TERRA-AQUA-MODIS_EDITION4A]. NASA Langley Atmospheric Science Data Center DAAC. Retrieved from `https://doi.org/10.5067/Terra+Aqua/CERES/SYN1degDay_L3.004A`. The surface ocean current datasets from GLORYS [GLOBAL_REANALYSIS_PHY_001_031] can be access provided by Copernicus Marine Environment Monitoring Service (CMEMS) via: `https://doi.org/10.48670/moi-00024`.

Acknowledgments

Funding for this work was provided by the Swedish National Space Agency, grant number 164/18 awarded to C.H. The authors would like to thank Birte Gülk and Dr. Aditya Narayanan from the Department of Marine Sciences, University of Gothenburg, Sweden; Dr. Malin Ödalen from GEOMAR Helmholtz-Zentrum für Ozeanforschung Kiel, Ocean Circulation and Climate Dynamics, Kiel, Germany; Dr. Stefanie Arndt from the Alfred Wegener Institute, Bremerhaven, Germany; and Julia Kukulies and Hui-Wen Lai from the Department of Earth Sciences, University of Gothenburg, Sweden, for their help with our data questions.

References

Ackley, S., Perovich, D., Maksym, T., Weissling, B., & Xie, H. (2020). Surface flooding of Antarctic summer sea ice. *Annals of Glaciology*, *61*(82), 117–126. doi: 10.1017/aog.2020.22

Andreas, E. L., Horst, T. W., Grachev, A. A., Persson, P. O. G., Fairall, C. W., Guest, P. S., & Jordan, R. E. (2010). Parametrizing turbulent exchange over summer sea ice and the marginal ice zone. *Quarterly Journal of the Royal Meteorological Society*, *136*(649), 927–943. doi: 10.1002/qj.618

Andreas, E. L., Persson, P. O. G., Grachev, A. A., Jordan, R. E., Horst, T. W., Guest, P. S., & Fairall, C. W. (2010). Parameterizing turbulent exchange over sea ice in winter. *Journal of Hydrometeorology*, *11*(1), 87–104. doi: 10.1175/2009JHM1102.1

Barber, D. G., & Massom, R. A. (2007). The role of sea ice in Arctic and Antarctic polynyas. *Elsevier oceanography series*, *74*, 1–54. doi: 10.1016/S0422-9894(06)74001-6

Bernardello, R., Marinov, I., Palter, J. B., Galbraith, E. D., & Sarmiento, J. L. (2014). Impact of Weddell Sea deep convection on natural and anthropogenic carbon in a climate model. *Geophysical Research Letters*, *41*(20), 7262–7269. doi: 10.1002/2014GL061313

Boisvert, L., Vihma, T., & Shie, C.-L. (2020). Evaporation from the Southern Ocean estimated on the basis of AIRS satellite data. *Journal of Geophysical Research: Atmospheres*, *125*(1), e2019JD030845. doi: 10.1029/2019JD030845

Boisvert, L. N., Boeke, R. C., Taylor, P. C., & Parker, C. L. (2022). Constraining Arctic Climate Projections of Wintertime Warming With Surface Turbulent Flux Obser-

vations and Representation of Surface-Atmosphere Coupling. *Frontiers in Earth Science*, *10*. Retrieved from https://www.frontiersin.org/article/10.3389/feart.2022.765304 doi: 10.3389/feart.2022.765304

Boisvert, L. N., Markus, T., & Vihma, T. (2013). Moisture flux changes and trends for the entire Arctic in 2003–2011 derived from EOS Aqua data. *Journal of Geophysical Research: Oceans*, *118*(10), 5829–5843. doi: 10.1002/jgrc.20414

Boisvert, L. N., Wu, D., Vihma, T., & Susskind, J. (2015). Verification of air/surface humidity differences from AIRS and ERA-Interim in support of turbulent flux estimation in the Arctic. *Journal of Geophysical Research: Atmospheres*, *120*(3), 945–963. doi: 10.1002/2014JD021666

Campbell, E. C., Wilson, E. A., Moore, G. K., Riser, S. C., Brayton, C. E., Mazloff, M. R., & Talley, L. D. (2019). Antarctic offshore polynyas linked to Southern Hemisphere climate anomalies. *Nature*, *570*(7761), 319–325. doi: 10.1038/s41586-019-1294-0

Carsey, F. (1980). Microwave observation of the Weddell Polynya. *Monthly Weather Review*, *108*(12), 2032–2044. doi: 10.1175/1520-0493(1980)108<2032:MOOTWP>2.0.CO;2

Cheng, Z., Pang, X., Zhao, X., & Tan, C. (2017). Spatio-temporal variability and model parameter sensitivity analysis of ice production in Ross Ice Shelf Polynya from 2003 to 2015. *Remote Sensing*, *9*(9), 934. doi: 10.3390/rs9090934

Cheon, W. G., & Gordon, A. L. (2019). Open-ocean polynyas and deep convection in the Southern Ocean. *Scientific reports*, *9*(1), 1–9. doi: 10.1038/s41598-019-43466-2

Comiso, J. C., Kwok, R., Martin, S., & Gordon, A. L. (2011). Variability and trends in sea ice extent and ice production in the Ross Sea. *Journal of Geophysical Research: Oceans*, *116*(C4). doi: 10.1029/2010JC006391

de Boyer Montégut, C., Madec, G., Fischer, A. S., Lazar, A., & Iudicone, D. (2004). Mixed layer depth over the global ocean: An examination of profile data and a profile-based climatology. *Journal of Geophysical Research: Oceans*, *109*(C12). doi: 10.1029/2004JC002378

Doelling, D. R., Loeb, N. G., Keyes, D. F., Nordeen, M. L., Morstad, D., Nguyen, C., ... Sun, M. (2013). Geostationary enhanced temporal interpolation for CERES flux products. *Journal of Atmospheric and Oceanic Technology*, *30*(6), 1072–1090. doi: 10.1175/JTECH-D-12-00136.1

Doelling, D. R., Sun, M., Nguyen, L. T., Nordeen, M. L., Haney, C. O., Keyes, D. F., & Mlynczak, P. E. (2016). Advances in geostationary-derived longwave fluxes for the CERES synoptic (SYN1deg) product. *Journal of Atmospheric and Oceanic Technology*, *33*(3), 503–521. doi: 10.1175/JTECH-D-15-0147.1

d'Ortenzio, F., Iudicone, D., de Boyer Montegut, C., Testor, P., Antoine, D., Marullo, S., ... Madec, G. (2005). Seasonal variability of the mixed layer depth in the Mediterranean Sea as derived from in situ profiles. *Geophysical Research Letters*, *32*(12). doi: 10.1029/2005GL022463

Drucker, R., Martin, S., & Kwok, R. (2011). Sea ice production and export from coastal polynyas in the Weddell and Ross Seas. *Geophysical Research Letters*, *38*(17). doi: 10.1029/2011GL048668

Dufour, C. O., Morrison, A. K., Griffies, S. M., Frenger, I., Zanowski, H., & Winton, M. (2017). Preconditioning of the Weddell Sea polynya by the ocean mesoscale and dense water overflows. *Journal of Climate*, *30*(19), 7719–7737. doi: 10.1175/JCLI-D-16-0586.1

Francis, D., Eayrs, C., Cuesta, J., & Holland, D. (2019). Polar cyclones at the origin of the reoccurrence of the Maud Rise Polynya in austral winter 2017. *Journal of Geophysical Research: Atmospheres*, *124*(10), 5251–5267. doi: 10.1029/2019JD030618

Francis, D., Mattingly, K. S., Temimi, M., Massom, R., & Heil, P. (2020). On the crucial role of atmospheric rivers in the two major Weddell Polynya events in 1973 and 2017 in Antarctica. *Science advances*, *6*(46), eabc2695. doi: 10.1126/sciadv.abc2695

Fujino, K., Lewis, E., & Perkin, R. (1974). The freezing point of seawater at pressures up to 100 bars. *Journal of Geophysical Research*, *79*(12), 1792–1797. doi: 10.1029/JC079i012p01792

Fusco, G., Budillon, G., & Spezie, G. (2009). Surface heat fluxes and thermohaline variability in the Ross Sea and in Terra Nova Bay polynya. *Continental Shelf Research*, *29*(15), 1887–1895. doi: 10.1016/j.csr.2009.07.006

Garric, G., & Parent, L. (2018). *Product user manual for global ocean reanalysis products GLOBAL-REANALYSIS-PHY-001-025* (Tech. Rep.). Retrieved from `http://cmems-resources.cls.fr/documents/PUM/CMEMS-GLO-PUM-001-025-011-017.pdf`

Gelaro, R., McCarty, W., Suárez, M. J., Todling, R., Molod, A., Takacs, L., ... others (2017). The modern-era retrospective analysis for research and applications, version 2 (MERRA-2). *Journal of climate*, *30*(14), 5419–5454. doi: 10.1175/JCLI-D-16-0758.1

Gordon, A. (1982, 01). Weddell Deep Water variability. *Journal of Marine Research*, *40*, 199-217.

Gordon, A. L., & Huber, B. A. (1990). Southern Ocean winter mixed layer. *Journal of Geophysical Research: Oceans*, *95*(C7), 11655–11672. doi: 10.1029/JC095iC07p11655

Gordon, A. L., Visbeck, M., & Comiso, J. C. (2007). A possible link between the Weddell Polynya and the Southern Annular Mode. *Journal of Climate*, *20*(11), 2558–2571. doi: 10.1175/JCLI4046.1

Grachev, A. A., Andreas, E. L., Fairall, C. W., Guest, P. S., & Persson, P. O. G. (2007). SHEBA flux–profile relationships in the stable atmospheric boundary layer. *Boundary-layer meteorology*, *124*(3), 315–333. doi: 10.1007/s10546-007-9177-6

Guo, G., Shi, J., Gao, L., Tamura, T., & Williams, G. D. (2019). Reduced sea ice production due to upwelled oceanic heat flux in Prydz Bay, East Antarctica. *Geophysical Research Letters*, *46*(9), 4782–4789. doi: 1029/2018GL081463

Haid, V., & Timmermann, R. (2013). Simulated heat flux and sea ice production at coastal polynyas in the southwestern Weddell Sea. *Journal of Geophysical Research: Oceans*, *118*(5), 2640–2652. doi: 10.1002/jgrc.20133

Hersbach, H., Bell, B., Berrisford, P., Hirahara, S., Horányi, A., Muñoz-Sabater, J., ... others (2020). The ERA5 global reanalysis. *Quarterly Journal of the Royal Meteorological Society*, *146*(730), 1999–2049. doi: 10.1002/qj.3803

Heuzé, C. (2021). Antarctic bottom water and North Atlantic deep water in CMIP6 models. *Ocean Science*, *17*(1), 59–90. doi: 10.5194/os-17-59-2021

Heuzé, C., Zhou, L., Mohrmann, M., & Lemos, A. (2021). Spaceborne infrared imagery for early detection of Weddell Polynya opening. *The Cryosphere*, *15*(7), 3401–3421. Retrieved from `https://tc.copernicus.org/articles/15/3401/2021/` doi: 10.5194/tc-15-3401-2021

Holland, P. R., & Kwok, R. (2012). Wind-driven trends in Antarctic sea-ice drift. *Nature Geoscience*, *5*(12), 872–875. doi: 10.1038/ngeo1627

Holte, J., & Talley, L. (2009). A new algorithm for finding mixed layer depths with applications to Argo data and Subantarctic Mode Water formation. *Journal of Atmospheric and Oceanic Technology*, *26*(9), 1920–1939. doi: 10.1175/2009JTECHO543.1

Hunke, E., Lipscomb, W., Jones, P., Turner, A., Jeffery, N., & Elliott, S. (2017). *CICE, The Los Alamos sea ice model* (Tech. Rep.). Los Alamos National Lab.(LANL), Los Alamos, NM (United States).

Huntemann, M., Heygster, G., Kaleschke, L., Krumpen, T., Mäkynen, M., & Drusch, M. (2014). Empirical sea ice thickness retrieval during the freeze-up period from SMOS high incident angle observations. *The Cryosphere*, *8*(2), 439–451. doi: 10.5194/tc-8-439-2014

Huot, P.-V., Kittel, C., Fichefet, T., Jourdain, N. C., Sterlin, J., & Fettweis, X. (2021). Effects of the atmospheric forcing resolution on simulated sea ice and polynyas off Adélie Land, East Antarctica. *Ocean Modelling*, *168*, 101901. doi: 10.1016/j.ocemod.2021.101901

Jardon, F. P., Vivier, F., Bouruet-Aubertot, P., Lourenço, A., Cuypers, Y., & Willmes, S. (2014). Ice production in Storfjorden (Svalbard) estimated from a model based on AMSR-E observations: Impact on water mass properties. *Journal of Geophysical Research: Oceans*, *119*(1), 377–393. doi: 10.1002/2013JC009322

Jena, B., Ravichandran, M., & Turner, J. (2019). Recent reoccurrence of large open-ocean polynya on the Maud Rise seamount. *Geophysical Research Letters*, *46*(8), 4320–4329. doi: 10.1029/2018GL081482

Johnson, K. S., Riser, S. C., Boss, E. S., Talley, L. D., Sarmiento, J. L., Swift, D. D., ... Russell, J. L. (2017). *Southern Ocean Carbon and Climate Observations and Modeling (SOCCOM) Float Data Archive* [dataset]. UC San Diego Library Digital Collections. Retrieved from `https://doi.org/10.6075/J0TX3C9X` doi: 10.6075/J0TX3C9X

Kacimi, S., & Kwok, R. (2020). The Antarctic sea ice cover from ICESat-2 and CryoSat-2: freeboard, snow depth, and ice thickness. *The Cryosphere*, *14*(12), 4453–4474. doi: 10.5194/tc-14-4453-2020

Kaufman, Z. S., Feldl, N., Weijer, W., & Veneziani, M. (2020). Causal interactions between Southern Ocean polynyas and high-latitude atmosphere–ocean variability. *Journal of Climate*, *33*(11), 4891–4905. doi: 10.1175/JCLI-D-19-0525.1

Kobayashi, S., Ota, Y., Harada, Y., Ebita, A., Moriya, M., Onoda, H., ... others (2015). The JRA-55 reanalysis: General specifications and basic characteristics. *Journal of the Meteorological Society of Japan. Ser. II*, *93*(1), 5–48. doi: 10.2151/jmsj.2015-001

Kusahara, K., Williams, G. D., Tamura, T., Massom, R., & Hasumi, H. (2017). Dense shelf water spreading from Antarctic coastal polynyas to the deep Southern Ocean: A regional circumpolar model study. *Journal of Geophysical Research: Oceans*, *122*(8), 6238-6253. doi: 10.1002/2017JC012911

Launiainen, J., & Vihma, T. (1990). Derivation of turbulent surface fluxes - An iterative flux-profile method allowing arbitrary observing heights. *Environmental Software*, *5*(3), 113–124. doi: 10.1016/0266-9838(90)90021-W

Lavergne, T., Piñol Solé, M., Down, E., & Donlon, C. (2021). Towards a swath-to-swath sea-ice drift product for the Copernicus Imaging Microwave Radiometer mission. *The Cryosphere*, *15*(8), 3681–3698. doi: 10.5194/tc-15-3681-2021

Lellouche, J.-M., Le Galloudec, O., Drévillon, M., Régnier, C., Greiner, E., Garric, G., ... others (2013). Evaluation of global monitoring and forecasting systems at Mercator Océan. *Ocean Science*, *9*(1), 57–81. doi: 10.5194/os-9-57-2013

Ludwig, V., Spreen, G., Haas, C., Istomina, L., Kauker, F., & Murashkin, D. (2019). The 2018 North Greenland polynya observed by a newly introduced merged optical and passive microwave sea-ice concentration dataset. *The Cryosphere*, *13*(7), 2051–2073. doi: 10.5194/tc-13-2051-2019

Lytle, V., & Ackley, S. (1996). Heat flux through sea ice in the western Weddell Sea: Convective and conductive transfer processes. *Journal of Geophysical Research: Oceans*, *101*(C4), 8853–8868. doi: 10.1029/95JC03675

Macdonald, G. J., Ackley, S. F., & Mestas-Nuñez, A. M. (2022). Evolution of the dynamics, area and ice production of the Amundsen Sea Polynya, Antarctica, 2016–2021. *The Cryosphere Discussions*, 1–32. Retrieved from `https://tc.copernicus.org/preprints/tc-2022-51/` doi: 10.5194/tc-2022-51

Marsland, S., & Wolff, J.-O. (2001). On the sensitivity of Southern Ocean sea ice to the surface freshwater flux: A model study. *Journal of Geophysical Research: Oceans*, *106*(C2), 2723–2741. doi: 10.1029/2000JC900086

Martin, S., Drucker, R. S., & Kwok, R. (2007). The areas and ice production of the western and central Ross Sea polynyas, 1992–2002, and their relation to the B-15 and C-19 iceberg events of 2000 and 2002. *Journal of Marine Systems*, *68*(1-2), 201–214. doi: 10.1016/j.jmarsys.2006.11.008

Martin, T., Park, W., & Latif, M. (2013). Multi-centennial variability controlled by Southern Ocean convection in the Kiel Climate Model. *Climate dynamics*, *40*(7), 2005–2022. doi: 10.1007/s00382-012-1586-7

Maykut, G., & McPhee, M. G. (1995). Solar heating of the Arctic mixed layer. *Journal of Geophysical Research: Oceans*, *100*(C12), 24691–24703. doi: 10.1029/95JC02554

Mchedlishvili, A., Spreen, G., Melsheimer, C., & Huntemann, M. (2022). Weddell Sea polynya analysis using SMOS–SMAP apparent sea ice thickness retrieval. *The*

Cryosphere, *16*(2), 471–487. doi: 10.5194/tc-16-471-2022

McPhee, M. G. (1992). Turbulent heat flux in the upper ocean under sea ice. *Journal of Geophysical Research: Oceans*, *97*(C4), 5365–5379. doi: 10.1029/92JC00239

McPhee, M. G., Kottmeier, C., & Morison, J. H. (1999). Ocean heat flux in the central Weddell Sea during winter. *Journal of Physical Oceanography*, *29*(6), 1166–1179. doi: 10.1175/1520-0485(1999)029<1166:OHFITC>2.0.CO;2

Melsheimer, C., & Spreen, G. (2019). *AMSR2 ASI sea ice concentration data, Antarctic, version 5.4 (NetCDF) (July 2012 - December 2018).* PANGAEA.[Date Accessed:2022-07-01]. doi: 10.1594/PANGAEA.898400

Menzel, W. P., Schmit, T. J., Zhang, P., & Li, J. (2018). Satellite-based atmospheric infrared sounder development and applications. *Bulletin of the American Meteorological Society*, *99*(3), 583–603. doi: 10.1175/BAMS-D-16-0293.1

Mohrmann, M., Heuzé, C., & Swart, S. (2021). Southern Ocean polynyas in CMIP6 models. *The Cryosphere*, *15*(9), 4281–4313. Retrieved from `https://tc.copernicus.org/articles/15/4281/2021/` doi: 10.5194/tc-15-4281-2021

Mohrmann, M., Swart, S., & Heuzé, C. (2022). Observed mixing at the flanks of Maud Rise in the Weddell Sea. *Geophysical Research Letters*, *49*(8), e2022GL098036. doi: 10.1029/2022GL098036

Monroe, E. E., Taylor, P. C., & Boisvert, L. N. (2021). Arctic Cloud Response to a Perturbation in Sea Ice Concentration: The North Water Polynya. *Journal of Geophysical Research: Atmospheres*, *126*(16), e2020JD034409. doi: 10.1029/2020JD034409

Morales Maqueda, M., Willmott, A., & Biggs, N. (2004). Polynya dynamics: A review of observations and modeling. *Reviews of Geophysics*, *42*(1). doi: https://doi.org/10.1029/2002RG000116

Nakata, K., Ohshima, K., & Nihashi, S. (2021). Mapping of Active Frazil for Antarctic Coastal Polynyas, With an Estimation of Sea-Ice Production. *Geophysical Research Letters*, *48*(6), e2020GL091353. doi: 10.1029/2020GL091353

Nicolaus, M., Arndt, S., Hoppmann, M., Krumpen, T., Nicolaus, A., & Bartsch, A. (2017). *Sea ice drift, surface temperature, and barometric pressure on sea ice from Surface Velocity Profiler measurements.* Alfred Wegener Institute, Helmholtz Centre for Polar and Marine Research, Bremerhaven. doi: 10.1594/PANGAEA.875652.

Nicolaus, M., Hoppmann, M., Arndt, S., Hendricks, S., Katlein, C., König-Langlo, G., ... A., B. (2017). *Snow height and air temperature on sea ice from Snow Buoy measurements.* Alfred Wegener Institute, Helmholtz Centre for Polar and Marine Research, Bremerhaven. doi: 10.1594/PANGAEA.875638.

Nihashi, S., & Ohshima, K. I. (2015). Circumpolar mapping of Antarctic coastal polynyas and landfast sea ice: Relationship and variability. *Journal of climate*, *28*(9), 3650–3670. doi: 10.1175/JCLI-D-14-00369.1

Nihashi, S., Ohshima, K. I., & Kimura, N. (2012). Creation of a heat and salt flux dataset associated with sea ice production and melting in the Sea of Okhotsk. *Journal of Climate*, *25*(7), 2261–2278. doi: 10.1175/JCLI-D-11-00022.1

Ohshima, K. I., Fukamachi, Y., Williams, G. D., Nihashi, S., Roquet, F., Kitade, Y., ... others (2013). Antarctic Bottom Water production by intense sea-ice formation in the Cape Darnley polynya. *Nature Geoscience*, *6*(3), 235–240. doi: 10.1038/ngeo1738

Ohshima, K. I., Nihashi, S., & Iwamoto, K. (2016). Global view of sea-ice production in polynyas and its linkage to dense/bottom water formation. *Geoscience Letters*, *3*(1), 1–14. doi: 10.1186/s40562-016-0045-4

Panofsky, H. A. (1984). Atmospheric turbulence. *Models and methods for engineering applications.*, *397*.

Parmiggiani, F. (2011). Multi-year measurement of Terra Nova Bay winter polynya extents. *The European Physical Journal Plus*, *126*(4), 1–7. doi: 10.1140/epjp/i2011-11039-3

Paţilea, C., Heygster, G., Huntemann, M., & Spreen, G. (2019). Combined SMAP–SMOS thin sea ice thickness retrieval. *The Cryosphere*, *13*(2), 675–691. doi: 10.5194/tc-13-675-2019

Petit, B., & Norro, A. (2000). Seasonal evolution of sea ice and oceanic heat flux in the Wed-

dell Sea. *Journal of marine systems*, *27*(1-3), 37–52. doi: 10.1016/S0924-7963(00)00060-9

Preußer, A., Ohshima, K. I., Iwamoto, K., Willmes, S., & Heinemann, G. (2019). Retrieval of wintertime sea ice production in Arctic polynyas using thermal infrared and passive microwave remote sensing data. *Journal of Geophysical Research: Oceans*, *124*(8), 5503–5528. doi: 10.1029/2019JC014976

Renfrew, I. A., King, J. C., & Markus, T. (2002). Coastal polynyas in the southern Weddell Sea: Variability of the surface energy budget. *Journal of Geophysical Research: Oceans*, *107*(C6), 16–1. doi: 10.1029/2000JC000720

Riser, S. C., Swift, D., & Drucker, R. (2018). Profiling floats in SOCCOM: Technical capabilities for studying the Southern Ocean. *Journal of Geophysical Research: Oceans*, *123*(6), 4055–4073. doi: 10.1002/2017JC013419

Roquet, F., Wunsch, C., Forget, G., Heimbach, P., Guinet, C., Reverdin, G., ... others (2013). Estimates of the Southern Ocean general circulation improved by animal-borne instruments. *Geophysical Research Letters*, *40*(23), 6176–6180. doi: 10.1002/2013GL058304

Rose, F. G., Rutan, D. A., Charlock, T., Smith, G. L., & Kato, S. (2013). An algorithm for the constraining of radiative transfer calculations to CERES-observed broadband top-of-atmosphere irradiance. *Journal of Atmospheric and Oceanic Technology*, *30*(6), 1091–1106. doi: 10.1175/JTECH-D-12-00058.1

Saha, S., Moorthi, S., Wu, X., Wang, J., Nadiga, S., Tripp, P., ... others (2014). The NCEP climate forecast system version 2. *Journal of Climate*, *27*(6), 2185–2208. doi: 10.1175/JCLI-D-12-00823.1

Small, R. J., Bacmeister, J., Bailey, D., Baker, A., Bishop, S., Bryan, F., ... others (2014). A new synoptic scale resolving global climate simulation using the Community Earth System Model. *Journal of Advances in Modeling Earth Systems*, *6*(4), 1065–1094. doi: 10.1002/2014MS000363

Spreen, G., Kaleschke, L., & Heygster, G. (2008). Sea ice remote sensing using AMSR-E 89-GHz channels. *Journal of Geophysical Research: Oceans*, *113*(C2). doi: 10.1029/2005JC003384

Swart, S., Campbell, E., Heuze, C., Johnson, K., Lieser, J., Massom, R., ... others (2018). Return of the Maud Rise polynya: Climate litmus or sea ice anomaly?[in "State of the Climate in 2017"]. *Bulletin of the American Meteorological Society*, *99*(8), S188–S189. doi: 10.1175/2018BAMSStateoftheClimate.1

Tamura, T., Ohshima, K. I., Fraser, A. D., & Williams, G. D. (2016). Sea ice production variability in Antarctic coastal polynyas. *Journal of Geophysical Research: Oceans*, *121*(5), 2967–2979. doi: 10.1002/2015JC011537

Tamura, T., Ohshima, K. I., & Nihashi, S. (2008). Mapping of sea ice production for Antarctic coastal polynyas. *Geophysical Research Letters*, *35*(7). doi: 10.1029/2007GL032903

Tamura, T., Ohshima, K. I., Nihashi, S., & Hasumi, H. (2011). Estimation of surface heat/salt fluxes associated with sea ice growth/melt in the Southern Ocean. *SOLA*, *7*, 17–20. doi: 10.2151/sola.2011-005

Tang, W., Qin, J., Yang, K., Zhu, F., & Zhou, X. (2021). Does ERA5 outperform satellite products in estimating atmospheric downward longwave radiation at the surface? *Atmospheric Research*, *252*, 105453. doi: 10.1016/j.atmosres.2021.105453

Taylor, P. C., Hegyi, B. M., Boeke, R. C., & Boisvert, L. N. (2018). On the increasing importance of air-sea exchanges in a thawing Arctic: A review. *Atmosphere*, *9*(2), 41. doi: 10.3390/atmos9020041

Thompson, L., Smith, M., Thomson, J., Stammerjohn, S., Ackley, S., & Loose, B. (2020). Frazil ice growth and production during katabatic wind events in the Ross Sea, Antarctica. *The Cryosphere*, *14*(10), 3329–3347. doi: 10.5194/tc-14-3329-2020

Thurman, H. V. (2002). *Essentials of oceanography*. Upper Saddle River, NJ :Prentice Hall.

Timmermann, R., Lemke, P., & Kottmeier, C. (1999). Formation and maintenance of a polynya in the Weddell Sea. *Journal of physical oceanography*, *29*(6), 1251–1264. doi:

10.1175/1520-0485(1999)029<1251:FAMOAP>2.0.CO;2

Tschudi, M., Meier, W. N., Stewart, J. S., Fowler, C., & Maslanik, J. (2019). *Polar Pathfinder Daily 25 km EASE-Grid Sea Ice Motion Vectors, Version 4.* Boulder, Colorado USA. NASA National Snow and Ice Data Center Distributed Active Archive Center. doi: 10.5067/INAWUWO7QH7B.

Tsujino, H., Urakawa, S., Nakano, H., Small, R. J., Kim, W. M., Yeager, S. G., ... others (2018). JRA-55 based surface dataset for driving ocean–sea-ice models (JRA55-do). *Ocean Modelling*, *130*, 79–139. doi: 10.1016/j.ocemod.2018.07.002

Untersteiner, N., Thorndike, A., Rothrock, D., & Hunkins, K. (2007). AIDJEX revisited: A look back at the us-canadian arctic ice dynamics joint experiment 1970-78. *Arctic*, *60*(3), 327–336. Retrieved from https://www.jstor.org/stable/40512908

von Albedyll, L., Hendricks, S., Grodofzig, R., Krumpen, T., Arndt, S., Belter, H. J., ... Haas, C. (2022). Thermodynamic and dynamic contributions to seasonal Arctic sea ice thickness distributions from airborne observations. *Elementa: Science of the Anthropocene*, *10*(1). doi: 10.1525/elementa.2021.00074

Walkington, I., & Willmott, A. (2006). A Coupled Coastal Polynya–Atmospheric Boundary Layer Model. *Journal of physical oceanography*, *36*(5), 897–913. doi: 10.1175/JPO2901.1

Weijer, W., Veneziani, M., Stössel, A., Hecht, M. W., Jeffery, N., Jonko, A., ... Wang, H. (2017). Local atmospheric response to an open-ocean polynya in a high-resolution climate model. *Journal of Climate*, *30*(5), 1629–1641. doi: 10.1175/JCLI-D-16-0120.1

West, A., Collins, M., Blockley, E., Ridley, J., & Bodas-Salcedo, A. (2019). Induced surface fluxes: a new framework for attributing Arctic sea ice volume balance biases to specific model errors. *The Cryosphere*, *13*(7), 2001–2022. doi: 10.5194/tc-13-2001-2019

Wetzel, P., Haak, H., Jungclaus, J., & Maier-Reimer, E. (2004). *The Max-Planck-Institute Global Ocean/Sea-Ice Model.* (Tech. Rep.). Retrieved from https://mpimet.mpg.de/fileadmin/models/MPIOM/DRAFT_MPIOM_TECHNICAL_REPORT.pdf

Williams, G., Bindoff, N., Marsland, S., & Rintoul, S. (2008). Formation and export of dense shelf water from the Adélie Depression, East Antarctica. *Journal of Geophysical Research: Oceans*, *113*(C4). doi: 10.1029/2007JC004346

Wilson, E. A., Riser, S. C., Campbell, E. C., & Wong, A. P. (2019). Winter upper-ocean stability and ice–ocean feedbacks in the sea ice–covered Southern Ocean. *Journal of Physical Oceanography*, *49*(4), 1099–1117. doi: 10.1175/JPO-D-18-0184.1

Wu, X., Budd, W., & Allison, I. (2003). Modelling the impacts of persistent Antarctic polynyas with an atmosphere–sea-ice general circulation model. *Deep Sea Research Part II: Topical Studies in Oceanography*, *50*(8-9), 1357–1372. doi: 10.1016/S0967-0645(03)00072-9

Xu, Y., Li, H., Liu, B., Xie, H., & Ozsoy-Cicek, B. (2021). Deriving Antarctic Sea-Ice Thickness From Satellite Altimetry and Estimating Consistency for NASA's ICESat/ICESat-2 Missions. *Geophysical Research Letters*, *48*(20), e2021GL093425. doi: 10.1029/2021GL093425

Yao, T., & Tang, C. (2003). The formation and maintenance of the North Water polynya. *Atmosphere-Ocean*, *41*(3), 187–201. doi: 10.3137/ao.410301

Yu, Y., & Rothrock, D. (1996). Thin ice thickness from satellite thermal imagery. *Journal of Geophysical Research: Oceans*, *101*(C11), 25753–25766. doi: 10.1029/96JC02242

Zhou, L., Heuzé, C., & Mohrmann, M. (2022). Early Winter Triggering of the Maud Rise Polynya. *Geophysical Research Letters*, *49*(2), e2021GL096246. doi: 10.1029/2021GL096246